Computerized Medical Imaging and Graphics 33 (2009) 369–376

Contents lists available at ScienceDirect

Computerized Medical Imaging and Graphics

journal homepage: www.elsevier.com/locate/compmedimag

A combined region growing and deformable model method for extraction of closed surfaces in 3D CT and MRI scans

M. del Fresno*, M. Vénere, A. Clausse

CIC-CNEA-CONICET and Universidad Nacional del Centro, Pinto 399, 7000 Tandil, Argentina

ARTICLE INFO

Article history:
Received 31 July 2008
Received in revised form 4 March 2009
Accepted 9 March 2009

Keywords:
Image segmentation
Region growing
Deformable surface models
Hybrid methods
MRI

ABSTRACT

Image segmentation of 3D medical images is a challenging problem with several still not totally solved practical issues, such as noise interference, variable object structures and image artifacts. This paper describes a hybrid 3D image segmentation method which combines region growing and deformable models to obtain accurate and topologically preserving surface structures of anatomical objects of interest. The proposed strategy starts by determining a rough but robust approximation of the objects using a region-growing algorithm. Then, the closed surface mesh that encloses the region is constructed and used as the initial geometry of a deformable model for the final refinement. This integrated strategy provides an alternative solution to one of the flaws of traditional deformable models, achieving good refinements of internal surfaces in few steps. Experimental segmentation results of complex anatomical structures on both simulated and real data from MRI scans are presented, and the method is assessed by comparing with standard reference segmentations of head MRI. The evaluation was mainly based on the average overlap measure, which was tested on the segmentation of white matter, corresponding to a simulated brain data set, showing excellent performance exceeding 90% accuracy. In addition, the algorithm was applied to the detection of anatomical head structures on two real MRI and one CT data set. The final reconstructions resulting from the deformable models produce high quality meshes suitable for 3D visualization and further numerical analysis. The obtained results show that the approach achieves high quality segmentations with low computational complexity.

1. Introduction

The role of the different image modalities, as computed tomography (CT) and magnetic resonance images (MRI), is no longer restricted to the simple task of inspection of the individual slices. Actually, the interest has extended toward the development of advanced applications to assist in numerous clinical practices, such as treatments or surgery planning, detection of tissues, fractures or tumors, image registration, etc. [1,2]. In particular, image segmentation is an interesting and useful topic in computer graphics and pattern recognition, being an essential process in image analysis.

Different segmentation techniques have been proposed in the literature [3,4]. In general, segmentation methods are based on the local properties of the image, particularly, discontinuity and similarity. Methods based on discontinuities are called boundary-based methods, whereas methods based on some similarity property are known as region-based methods. Boundary-based algorithms search for the edges between regions in the image, by detecting abrupt grey level discontinuities and trying to connect the resulting edges to closed regions afterward [5]. These methods work well on datasets with good contrast, but their spatial-variation nature makes them extremely sensitive to noise or blurred object. The alternative is provided by deformable models, which are based on the evolution of manifolds – curves (in 2D) or surfaces (in 3D) – that are forced to evolve attracted by the region borders by minimizing appropriate energy functions [6]. Unlike voxel-based methods, these models can be applied over continuum domains, achieving subpixel (or subvoxel) precisions. Region-growing (RG) algorithms, particularly the well-known seeded region growing [7], have received special attention because it constitutes a powerful and flexible approach to image segmentation, aimed to the search of homogeneous regions inside the image based on connectivity and similarity properties among the voxels. Basically, region growing operates by merging the nearby voxels that meet a given homogeneity criterion, starting from an initial set of points, known as "seeds". This approach offers several advantages over conventional segmentation techniques. Instead of identifying boundaries, region growing operates always on closed regions in each step of the algorithm, and thus avoids further post-processing to recover the boundaries of disconnected objects. The algorithm is also more stable with respect to noise, and region membership can be based on multiple criteria, facilitating the simultaneous

* Corresponding author. Tel.: +54 2293 439690; fax: +54 2293 439690.
E-mail address: mdelfres@exa.unicen.edu.ar (M. del Fresno).

0895-6111/$ – see front matter © 2009 Elsevier Ltd. All rights reserved.
doi:10.1016/j.compmedimag.2009.03.002

consideration of several features from the image data, and the introduction of eventual *a priori* knowledge about the structures to be segmented.

Furthermore, a large number of hybrid algorithms that combine the advantages of different methods have been proposed. Particularly, considering the complementary nature of the boundary-based and region-based information, it is possible to integrate both methods yielding more accurate segmentation results than when they are applied separately [8–11]. The latter is especially important for medical images where segmentation is generally considered a very difficult problem, mainly due to overlapping intensities, anatomical complexity and variability in shape and size, let aside the usual limitations in the imaging equipment or input data (noise perturbations, intensity inhomogeneities, partial volume effect and low contrast).

In a variety of applications of three-dimensional (3D) image processing one would like to segment closed substructures of the image and create a compact geometrical representation of the boundary surfaces. The most popular method to achieve this goal is marching cubes [12], which constructs a triangular mesh that approximates the location of an isosurface in the volumetric data. This algorithm is fast and can usually detect well-defined boundaries. However, this technique do not guarantee the creation of closed surfaces and often fail to resolve complex or noisy boundaries, generating topology errors such as small handles or holes on the computed isosurface [13,14].

Region growing is a powerful method to tackle problematic segmentations, although the final reconstructions sometimes do not meet the required standards. This is especially difficult in medical images where the transition between objects of interests is often diffuse. Actually, the main limitation of region-growing algorithms is its discrete character (*i.e.*, the finest resolution is the elemental voxel). Therefore, the resulting surface models usually present discontinuous steps, which not only are not natural but are also inconvenient to support further scientific calculations, such as stress numerical analysis, mass and thermal transfer, surface chemical reactions, etc.

On the other hand, deformable models are well-known segmentation methods to achieve smooth and precise geometrical representations of surface boundaries [6]. However, the main limitation of traditional deformable models is their dependence on the required initial guess, which should be sufficiently close to the final solution in order to achieve good results. Because of that, deformable models generally fail to segment 3D objects with complex surface structures leading to over smoothed final segmentations. Several proposals were presented to overcome this limitation trying to improve the initialization task, with partial successes, the general problem still remaining an open problem. Cohen [15] proposes the uses of "balloons", introducing a numerical "pressure" that prevents that the model were trapped in local minima. This method improves the sensitivity to initial conditions, but the model hardly adapts to complex shapes. Xu and Prince [16] define a "gradient vector flow" to treat the forces external acting on the snakes, which ensures that the model is driven to the object border. McInerney and Terzopoulos [17] use the model T-snakes that in certain way improves the limitations of ordinary snakes. However the extension of T-snakes to 3D involves much complex algorithms and raises several non-trivial geometrical issues, due to the calculation of intersections and reparametrizations of the model [18]. Strauss et al. [13] propose the variant Dual-T-snakes, defining two interconnected snakes expanding and contracting toward the object border, initializing the model by means of marching cubes [12]. The latter unfortunately do not always arrive to good approximations and the results are too sensitive to the resolution of the base mesh. Finally, Chen and Metaxas [14] propose a hybrid method, initializing the deformable model with marching cubes combined in this case with morphological operators to avoid topological errors, like holes.

In this paper, a methodology for the detection and modeling of surfaces contained in 3D images is proposed, based on the integration of a region-growing algorithm and deformable models. This approach follows the recent trend to define hybrid methods taking advantage of different segmentation strategies [10]. The procedure implements a two-step region-growing strategy, which uses region and edge information to generate appropriate inputs for a suitable surface model. The hybrid method is capable of converging to the solution in a small number of steps without significant user intervention, achieving surface meshes of great quality with a subvoxel accuracy.

2. Description of the method

2.1. Two-stage region-growing algorithm

The input of the segmentation process is a 3D grey digital image represented by a intensity field $I(x, y, z)$ defined in a space discretized in voxels, $v(x, y, z)$, individually associated with intensity values according to the image modality and the acquisition technique.

Region growing (RG) is a simple and flexible method for image segmentation that allows the detection of the regions of interest starting from one or more initial seed points inside each of them. Although there are several approximations to provide automatic seeds [8,19], the generalized practice involves the direct expert intervention [20]. Typically, several seeds should be specified inside each region of interest, especially when the objects have complex structures or wide contrasts. In what follows the seed points are assumed to be provided by an expert user through a graphic interface that facilitates the exploration of the image. Starting from each seed the growing processes incorporates the voxels adjacent to the evolving border until no more adjacent voxels satisfying some criterion of similarity with the segmented object are found. The output of the process is sets of connected voxels representing the regions of interest.

In general, RG is appropriate for segmentation of complex volumetric objects since voxels of a same region can be disconnected in one slice, while maintaining linkage through adjacent slices in the three-dimensional structure. RG showed good results in segmenting blood vessels in MRA [21,22], vascular trees in CT angiography [23] or in radiographic data [24], human airways [25,26] and brain in MRI [27–29]. The latter is especially challenging due to the numerous fissures and circumvolutions that should be accurately isolated.

In this section, a two-step RG algorithm is described, which can define clearly objects even with diffuse borders while avoiding merging of incompatible regions through connecting "bridges".

2.1.1. First growing stage

The similarity criterion used in the first growing stage is based on the comparison of voxel intensities. Since certain noise or heterogeneities are always expected in real images, this criterion should be applied within certain tolerance. An appropriate tolerance band can be established using the average and the standard deviation of the intensity of the seeds' neighborhoods.

Let us consider the set $S(r)$ of all voxels r-neighboring any seed defined in a given region (with 26-conectivity). The characteristic intensity $CI(r)$ and standard deviation $\sigma(r)$ of the region are calculated as:

$$CI(r) = \frac{1}{N(r)} \sum_{v \in S(r)} I(v) \quad (1)$$

$$\sigma(r) = \sqrt{\frac{1}{N(r)} \sum_{v \in S(r)} [I(v) - CI(r)]^2} \quad (2)$$

where $N(r)$ is the number of voxels contained in $S(r)$ and k is an appropriate constant parameter that will be used later for performance tuning.

A generic voxel v is declared belonging to a certain region if the following inequality is satisfied:

$$s_v(k, r) = \frac{1}{k} \left\langle \frac{\left| I(v') - IC(r) \right|}{\sigma(r)} \right\rangle \leq 1 \quad (3)$$

where $\langle \bullet \rangle$ stands for the average of dissimilarity from the characteristic intensity over the voxels v' in the r-neighborhood of v, referring to the tolerance $k\sigma(r)$.

The growing process evolves in an iterative way according to a breadth first search strategy (BFS). An auxiliary FIFO list L is associated to each region of interest R_i, which initially includes the seeds provided for that region. The growing algorithm proceeds as follows:

Algorithm. Segmentation by region growing
Insert the seed voxels into the L list
while L is not empty
  remove the first voxel v_r from L
  label v_r as included in R_i
  for each non-visited neighbor v of v_r test similarity:
    if $(s_v(k_1, r) \leq 1)$
      insert v in L
    else
      label v_r as a boundary voxel
      insert v_r in *RG-list*
    endif
  endfor
endwhile

Finally, in order to provide information for the second segmentation step, the position of the final frontier is stored. For that purpose, when a voxel is discarded, the previously included voxel is appended to a *RG-list* of boundary points.

2.1.2. Second growing step

The initial growing process leads to acceptable results regarding the avoidance of overflowing problems. However, the borders of the regions are only crudely defined and may be slightly distant of the natural borders of the objects. In order to tackle this issue, a second refining growing step is applied – called "push" – that makes use of information of the intensity gradients.

The growing process is resumed from the voxels in the *RG-list* provided by the first step. The push process is analogous to the first step – *i.e.*, there is an acceptance criterion – the difference being that, taking advantage that the region is close to the object boundary, the tolerances are relaxed and an additional condition is imposed related to the intensity gradients typical of the region borders. The additional criterion requires the calculation of a gradient metric in a r-neighborhood ($r \geq 1$) of each visited voxel $v = (x, y, z)$, which is defined as:

$$grad_v(r) = \max\{Gx_v(r), Gy_v(r), Gz_v(r)\} \quad (4)$$

where

$$\left.\begin{aligned} Gx_v(r) &= \frac{1}{r} \sum_{i=1}^{r} |I(x+i, y, z) - I(x-i, y, z)| \\ Gy_v(r) &= \frac{1}{r} \sum_{j=1}^{r} |I(x, y+j, z) - I(x, y-j, z)| \\ Gz_v(r) &= \frac{1}{r} \sum_{k=1}^{r} |I(x, y, z+k) - I(x, y, z-k)| \end{aligned}\right\} \quad (5)$$

Given a weight coefficient, pg, valued between 0 and 1, and a precomputed value, max_gr, corresponding to the maximum gradient according to the image intensities, a voxel v can be considered inside the region if it satisfies:

$$grad_v(r) \leq pg \cdot \max\_gr \quad (6)$$

That is, in the second stage, in order to include a candidate voxel to the region, Eqs. (3) and (6) should be satisfied. The analysis of the local neighborhood slightly increases the computational cost, but it usually prevents from segmentation problems due to noise and leakage toward other regions. Moreover, the neighborhood thresholding ensures connectivity within regions.

In addition, the algorithm offers the possibility to fix the number of allowed levels in the BFS trajectory during the push procedure, which is useful to interactively control the growing process. This growing produces a depth-limited search (DLS) that is an interesting alternative to control channeling, specially in dealing with very noisy images or diffuse boundaries.

2.2. Final surface modeling

Once a connected set of voxels representing the hull of a region is determined, the final step is the modeling of the surface manifold. The procedure recommended to achieve this goal is to apply deformable models such as snakes, which lead to soft geometrical representations provided that the initial guess is close to the final surface.

2.2.1. Initialization of the deformable model

A *snake* is defined as an elastic curve (in 2D) or surface (in 3D) evolving from its initial position driven by internal and external forces. A snake surface is digitally represented by a triangular mesh defined by a set of vertexes $s_i(t, x_i, y_i, z_i)$, where t is the time and i is the vertex index.

Instead of using a user-defined initial surface as in traditional approaches, the geometry of the deformable model is constructed in our case using the *RG-list* of boundary voxels provided by the region growing process. A procedure to generate a hole-free surface mesh without local irregularities, while preserving the global topology of the region frontier is applied.

The algorithm starts by determining the faces of the voxels of *RG-list* corresponding to the region boundary (*i.e.*, those faces separating a voxel belonging to the region and an outsider voxel). In each of the boundary faces, two triangles are conformed labeling its vertexes counterclockwise (seen from the region) in order to ensure a close and oriented mesh. The resulting surface will have step discontinuities, since the triangles are perpendicular to each other (Fig. 1a). Following Taubin [30], the mesh is smoothed apply-

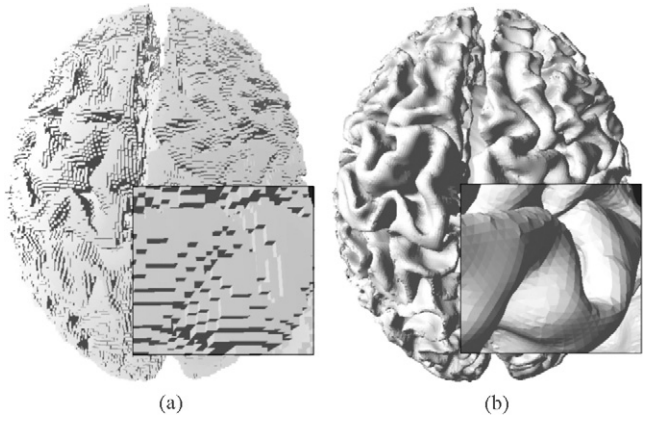

Fig. 1. Surface meshes generated by RG: (a) original, (b) after filter smoothing.

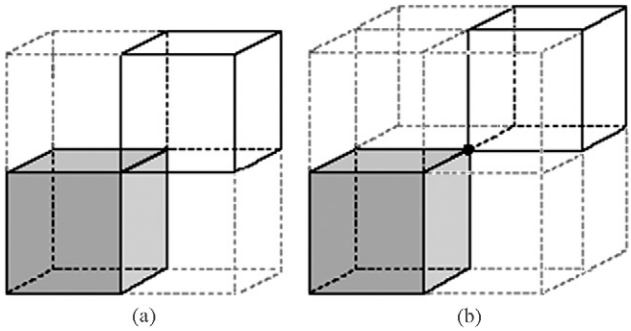

Fig. 2. Conflicting configurations (dashed voxels are absent) with voxels connected only by: (a) an edge, (b) a vertex.

ing a filter on each vertex. However, the filter fails where two or more voxels are "weakly connected" (*i.e.*, only share a single vertex or edge as shown in Fig. 2), which can lead to undesirable effects on the surface topology. To avoid this inconvenience, the occurrence of conflicting voxels arrangements should be checked during the generation of the initial mesh, solving them by relabeling the common vertexes in one of the conflicting triangles. The mentioned post-processing results in smoothed and hole-free surfaces without irregularities, while preserving the main topological information of the detected components, avoiding the drawbacks of conventional approaches based on isosurfaces [12–14]. The resulting model is a suitable initial guess for the fitting of deformable models.

2.2.2. Evolution of the deformable model

Different techniques were proposed for the evolution of the snake, such as finite differences, finite elements or dynamic programming [6,31,32]. In our case, the formulation proposed by McInerney and Terzopoulos [18] is applied, where each vertex $\boldsymbol{s}_i$ of the snake mesh evolves according to the following motion equation:

$$\gamma_i \frac{d\boldsymbol{s}_i}{dt} - a\boldsymbol{\alpha}_i(t) + b\boldsymbol{\beta}_i(t) = q\boldsymbol{\rho}_i(t) + p\boldsymbol{f}_i(t) \tag{7}$$

where $\boldsymbol{\alpha}_i(t)$, $\boldsymbol{\beta}_i(t)$, $\boldsymbol{\rho}_i(t)$ and $\boldsymbol{f}_i(t)$ are the tension, flexion, inflation and external forces respectively, and γ_i is a damping coefficient.

The internal energy simulates the characteristics of an elastic membrane. The internal tension and flexion acting on the vertex $\boldsymbol{s}_i$ represent the snake resistance to stretching and bending respectively, and are calculated as:

$$\boldsymbol{\alpha}_i(t) = \frac{1}{m}\sum_{j\in N(i)} \boldsymbol{s}_j(t) - \boldsymbol{s}_i(t) \tag{8}$$

$$\boldsymbol{\beta}_i(t) = \frac{1}{m}\sum_{j\in N(i)} \boldsymbol{\alpha}_j(t) - \boldsymbol{\alpha}_i(t) \tag{9}$$

where $N(i)$ is the set of nodes $\boldsymbol{s}_j$ neighboring the node $\boldsymbol{s}_i$ and m is the number of these neighbors. The respective derivatives correspond to the Laplacian and the squared Laplacian and they are approximated using the umbrella operator by considering the local mesh topology at the node $\boldsymbol{s}_i$.

The inflation $\boldsymbol{\rho}_i$ and the external force $\boldsymbol{f}_i$ are calculated as:

$$\boldsymbol{\rho}_i(t) = F(I(\boldsymbol{s}_i(t))\boldsymbol{n}_i(t) \tag{10}$$

where $\boldsymbol{n}_i$ is the unitary vector normal to the surface at node $\boldsymbol{s}_i$ and F is a binary function relating $\boldsymbol{\rho}_i$ to the intensity field I:

$$F(I(\boldsymbol{s}_i(t)) = \begin{cases} +1 & \text{if } \dfrac{|I(\boldsymbol{s}_i) - CI(r)|}{k\sigma(r)} \le 1 \\ -1, & \text{otherwise} \end{cases} \tag{11}$$

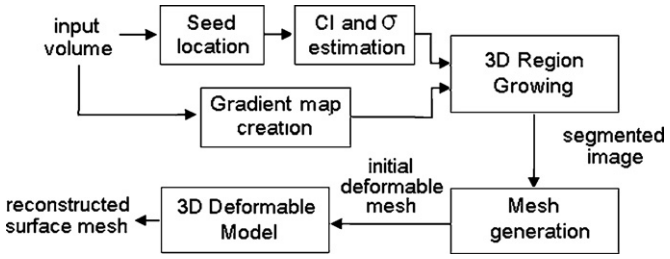

Fig. 3. Flowchart of the 3D segmentation hybrid method.

In other words, F takes the value 1 when the intensity $I(\boldsymbol{s}_i)$ is bounded within $k\sigma$ from the characteristic intensity, and −1 otherwise. The parameter k is the same as the one used in Eq. (3).

The local external force which contains the expansion of the snake at significant edges, acts in each node emulating a potential gradient:

$$\boldsymbol{f}_i(t) = G[\varphi(\boldsymbol{s}_i)] \tag{12}$$

where the gradient vector G is calculated using Eqs. (5), and the potential φ is defined as:

$$\varphi(\boldsymbol{s}_i) = -grad[FI(\boldsymbol{s}_i)] \tag{13}$$

The scalar gradient $grad[\cdot]$ being given by Eq. (4), and $FI(\boldsymbol{s}_i)$ is the intensity $I(\boldsymbol{s}_i)$ smoothed with a Gaussian filter [5].

Since the initial guess provided by the growing process is a close approximation of the final model, Eq. (7) can be solved directly by applying an explicit first-order Euler scheme:

$$\boldsymbol{s}_i^{(t+\Delta t)} = \boldsymbol{s}_i^{(t)} - \frac{\Delta t}{\gamma}(-a\boldsymbol{\alpha}_i^{(t)} + b\boldsymbol{\beta}_i^{(t)} - q\boldsymbol{\rho}_i^{(t)} - p\boldsymbol{f}_i^{(t)}) \tag{14}$$

provided that the time steps are sufficiently small. The iteration proceeds until the displacement of every node does not exceeds a given convergence value. The advantage of using the RG result to initialize the snake is that the deformation is then limited to minor perturbations requiring a few iteration steps. The deformable mesh is composed of subvoxel triangular elements, so the final segmentation has subvoxel accuracy and yields a smooth surface representation, matching concavities and convexities that may be present on complex geometries. Fig. 3 shows the flowchart of the 3D segmentation method.

3. Experimental results

The described methodology was applied to the detection and surface retrieval of anatomical structures on simulated and real medical images. The segmentation system was developed in Visual C++ as an object-oriented windows-based software, with an interactive user interface. All tests were made on a Pentium(R) D 2.8 GHz PC, with 2 Gb of RAM and a GeForce 7300 GS graphics card, under Windows XP platform.

3.1. Segmentations of simulated images

A sensitivity analysis of the influence of the main control parameters on the segmentation results was performed using the BrainWeb simulated brain dataset available at the web site http://www.bic.mni.mcgill.ca/brainweb of the McConnell Brain Imaging Center at Montréal Neurological Institute (MNI). This image is a simulated MR brain data, which provide 3D image simulations with 1 mm × 1 mm of interslice resolution, with slice thicknesses ranging from 1 to 9 mm. The size of all analyzed images is 181 × 217 × 181 voxels of 1 mm^3 each. This MRI simulator helps us to adjust two main parameters: noise level (NL) and intensity non-uniformity (INU). Moreover, a ground truth of the model is provided

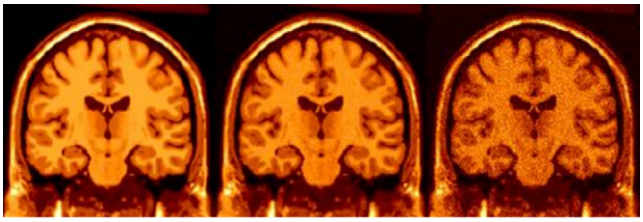

Fig. 4. MRI T1-weighted images from the Brainweb simulator with different noise level: (a) noise-free, (b) with moderate noise (5%), (c) with high noise (9%).

by the simulator by means of membership functions, indicating the probability of each voxel belonging to different tissues [33]. Therefore, this database serves as test model of the proposed algorithm on images of different qualities and provides a quantitative way to assess its performance through a computational phantom. The segmentation method was tested on MRI images weighted in T1, considered a practical standard of brain images [11]. Fig. 4 shows the images chosen, with 0%, 5% and 9% noise background. The algorithm was applied to detect white matter (WM), comparing the results with the classification provided by the simulator in each case.

In order to assess the results an Average Overlap Metric (AOM) was applied, which has been used in numerous works as a quantitative indicator of segmentation quality [11,34]:

$$\mathrm{AOM} = \frac{|V_i \cap V_a|}{1/2\left[\left|V_i\right| + |V_a|\right]} \tag{15}$$

where V_i and V_a are the sets of voxels classified as the corresponding tissue in the simulator phantom and by the algorithm, respectively. That is, AOM is the number of voxels simultaneously contained in both segmentations relative to average of voxels of both segmentations. This metric reaches a value of 1.0 for results that are very similar and is near 0.0 when they share no similarly classified voxels.

In addition to AOM, the following indicators were used:

$$\left.\begin{aligned} \mathrm{CP} &= \frac{|V_i \cap V_a|}{|V_i \cup V_a|} \\ \mathrm{FNP} &= \frac{|V_i - V_a|}{|V_i \cup V_a|} \\ \mathrm{FPP} &= \frac{|V_a - V_i|}{|V_i \cup V_a|} \end{aligned}\right\} \tag{16}$$

where CP is the fraction of coincidences between the ideal segmentation V_i and the obtained by the algorithm V_a, FNP is the ratio of false negatives and FPP is the ratio of false positives.

Fig. 5 shows the sensitivity of the performance metrics to variations of the growing tolerance parameter k defined in Eq. (3), for $r = 2$. As k increases the number of false negatives decreases, but for values of k larger than certain threshold false positives begin to appear in the results. This competition produces the curve of AOM showing an optimum value around $k = 2$ for the image free of noise, $k = 2.5$ for 5% noise level and $k = 1.5$ for 9% noise level (Fig. 6). It can be seen that as expected the presence of noise in the image deteriorate the performance, although the general trend persists. Fig. 7 shows the influence of the parameter r, that is the dimension of the local neighborhood. The best performance are achieved for $r = 1$, for which values of AOM higher than 0.94 are achieved in an image with low noise ($\leq$5%) and 0.92 with a noisy image (9%). As r increases the performance indicators deteriorate as the number of false positives and negatives increases. Also note that when the voxels are assessed in isolation (*i.e.*, $r = 0$) the resulting segmentations are poor (AOM ranging from 0.71 to 0.81 depending on the noise level).

Fig. 8 shows the results of the segmentation of WM of the brain on a noise-free MRI image from the Brainweb site. The segmentation with the RG algorithm was applied using $k = 2$ and $r = 1$ to create

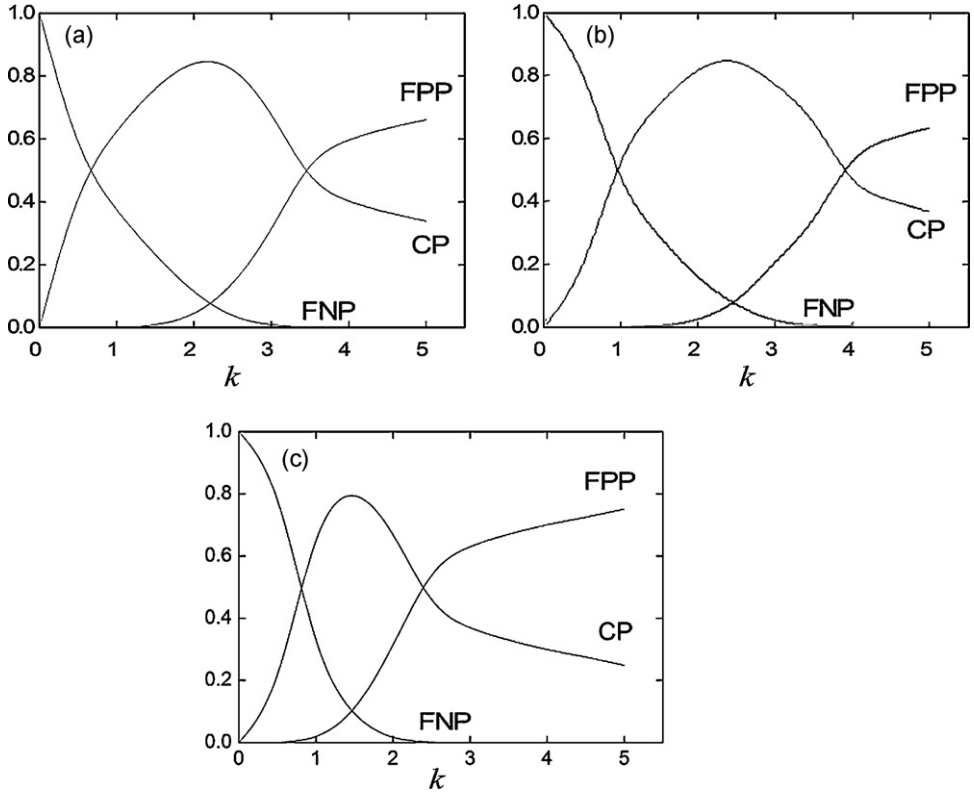

Fig. 5. Dependence of the segmentation performance on the tolerance parameter k in uniform images: (a) 0%, (b) 5% and (c) 9%.

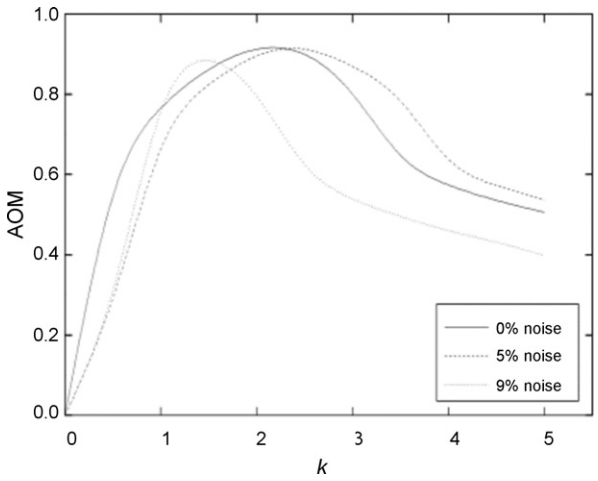

Fig. 6. Comparison of segmentation performances on the tolerance parameter k for different noise levels of the image.

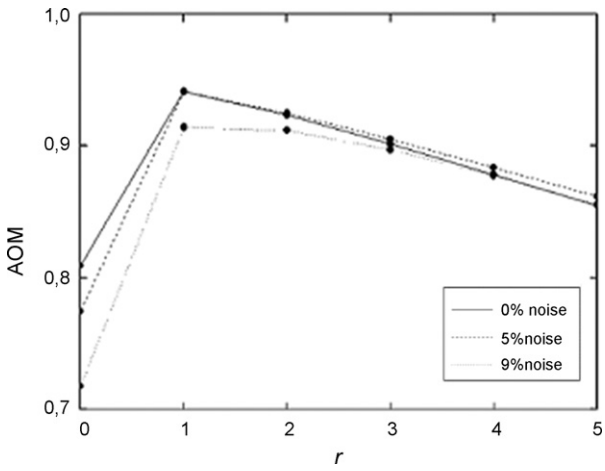

Fig. 7. Dependence of the segmentation performance on the parameter r.

the initial mesh for the deformable model (Fig. 8a). The parameters used in the latter were: $a = 30, b = 20, p = 3, q = 5, \Delta t = 0.005$. Different views of the reconstructed surface obtained after the application of the segmentation algorithm are shown in Fig. 8b–d. It can be seen that the algorithm performs very well in dealing with the complex structure of the brain surface, progressing into the convoluted surface.

In order to test the robustness of the proposed algorithm, the method was also applied to simulated images with moderate noise (5%) and high noise (9%). In both cases the optimum set of RG parameters was chosen (Figs. 6 and 7) and the resulting mesh was used as input of the deformable model. The results show that, in spite of the anatomical complexity of the segmented object, the method can achieve high quality results. Tables 1 and 2 summarize typical values of the quality indicators calculated in images with different levels of noise and inhomogeneities. In particular, although the segmentation quality logically deteriorates in the presence of noise and variations in intensity, the robustness of the present algorithm is highly satisfactory even comparing with the results of other segmentation strategies, like [11].

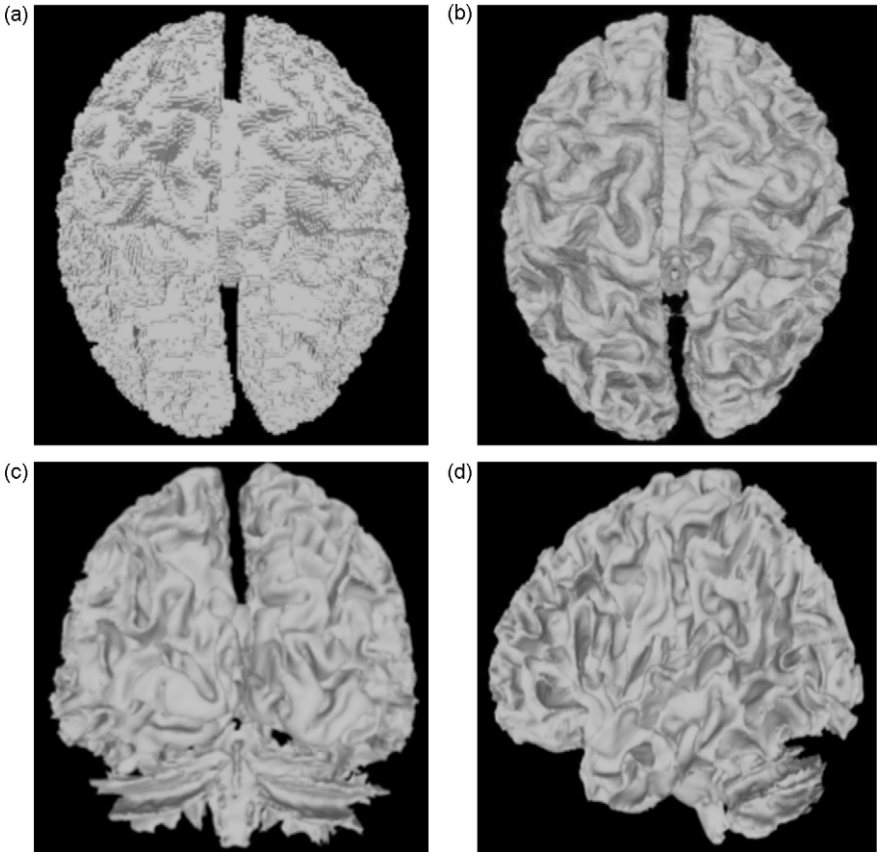

Fig. 8. Surface renderings of a reconstructed brain surface from a noise-free 3D image ($a = 30$, $b = 20$, $p = 3$, $q = 5$ and $\Delta t = 0.005$): (a) Initial guess from the RG segmentation, (b) axial view of the final segmentation, (c) coronal view of the final segmentation, (d) sagital view of the final segmentation.

Table 1
AOM performance metrics for segmentations on simulated T1-weighted MRI data (BrainWeb) in different situations of noise level (NL) and intensity non-uniformity (INU).

AOM	NL = 0%	NL = 5%	NL = 9%
INU = 0%	0.94	0.94	0.91
INU = 20%	0.92	0.92	0.90
INU = 40%	0.89	0.89	0.87

Table 2
Proportions of coincidence (PC), false negatives (PFN) and false positives (PFP) for the WM segmentation in images with different degrees of noise level (NL) and intensity non-uniformity (INU).

		Noise 0%	Noise 5%	Noise 9%
INU = 0%	PC	0.889	0.889	0.841
	PFN	0.096	0.056	0.063
	PFP	0.015	0.055	0.096
INU = 20%	PC	0.853	0.855	0.826
	PFN	0.049	0.060	0.090
	PFP	0.098	0.085	0.084
INU = 40%	PC	0.799	0.799	0.775
	PFN	0.141	0.129	0.150
	PFP	0.060	0.072	0.075

Regarding the computational performance, working with a Pentium(R) D 2.8 GHz, 2 Gb RAM, the RG segmentation of the brain takes 5 s, the initial deformable mesh generation 20 s, and the final mesh (463.000 nodes) takes 75 s for about 70 steps of deformation. The total segmentation time of the brain is about 100 s, which is considerable shorter than the reported for other techniques for the same data set [14,28].

3.2. Segmentation of real images

In addition to the tests on synthetic images, the algorithm was applied to the detection of anatomical structures on real MRI and CT images. One of the experiments corresponds to the segmentation of brain in a head MRI of $256 \times 256 \times 85$ voxels. The RG parameters are $r = 1$ and $k = 1.5$, resulting a 370.500 vertex mesh, which was further conformed to resolve conflicts, then smoothed, and finally used as initial guess of the deformable model. The latter required 50 iterations to reach the final result, using the parameters $a = 10$, $b = 10$, $p = 3$, $q = 5$ and $\Delta t = 0.001$. The computation time was 10 s for RG, 35 s for filtering and smoothing, and 65 s for the deformable model. We also segmented the brain tumor in other MRI data set of $256 \times 256 \times 124$ voxels. The RG parameters to obtain the initial mesh were $r = 1$ and $k = 1.5$. The deformable model required 25 iterations to reach the final result, using the parameters $a = 5$, $b = 3$, $p = 2$, $q = 5$ and $\Delta t = 0.005$.

CT images and other structures with different anatomical complexity were also tested with the present method. For example, a CT image of $256 \times 256 \times 125$ voxels was processed to detect the regions corresponding to the brain, skull and the external tissue. In this case, the RG segmentation of the skull required several internal seeds, but the final result could be reached readily with the evaluation of individual voxels (*i.e.*, $r = 0$) since the bone density is very different from the surrounding tissues.

4. Conclusions

A method for segmentation of internal structures in 3D images was presented. The method combines RG and deformable models algorithms, and was tested in different anatomical structures in head MRI and CT scans. The proposed method has several advantages compared with previous segmentation strategies. One of the most important improvements is that the algorithm always generates closed and oriented surface meshes that enclose the segmented regions. The initial RG segmentation provides a convenient detection of the structures of interest with a user intervention limited to the selection of a few seeds to identify the regions. The growing process incorporates information of the local neighborhood properties of each voxel of the region boundary, which substantially reduces the treatment of noisy images and precludes the channeling through narrow gaps between regions. Using the segmentations obtained with the RG procedure as initialization of deformable models, smooth mesh representations of surface structures of high geometrical complexity can be retrieved within tens of iterations. The present approach offers an alternative to other proposals that apply marching cubes to generate initial meshes for deformable models, which are bound to the typical limitations of the latter. Indeed, the classical issue of initializing deformable models – particularly of active surfaces – could be solved by the construction of a surface tight to the solution manifold by means of region-growing procedures. In this way, the deformation of the snake model is constraint to minor smoothing perturbations, reducing substantially the computational complexity. In the very special cases of strange structures, such as fractal like, the user can intervene in the process modifying the RG solution.

The model was tested on the segmentation of complex anatomical 3D structures from a standard synthetic phantom, and one CT and two MRI real scans. Quantitative assessments of the simulated brain images for the segmentation of white matter show excellent performances exceeding 90%, substantially minimizing the fault negatives and positives. The final representations resulting from the deformable models produce high quality meshes easy to visualize in 3D and suitable for supporting further numerical analysis.

The present method, like other hybrid methods developed for image segmentation [14], can be easily implemented using the Insight ToolKit (ITK) [35], a segmentation and registration toolkit which includes various high-level and low-level image processing algorithms. The authors hope that the different modules of the present methodology can provide new alternatives for the development of useful applications of image segmentation techniques.

References

[1] Duncan J, Ayache N. Medical image analysis: progress over two decades and challenges ahead. IEEE Transactions on Pattern Recognition and Machine Intelligence 2000;22(1):85–106.
[2] Imielinska C, Molholt P. Incorporating 3D virtual anatomy into the medical curriculum. Communications of the ACM 2005;48(2.):49–54.
[3] Pham D, Xu C, Prince J. A survey of current methods in medical image segmentation. Annual Review of Biomedical Engineering 2000;2:315–37.
[4] Lucchese L, Mitra S. Color image segmentation: a state-of-the-art survey, image processing, vision, and pattern recognition. The Indian National Science Academy 2001;67(2):207–21.
[5] Castleman K. Digital image processing. NJ: Prentice Hall; 1996.
[6] Kass M, Witkin A, Terzopoulos D. Snakes: active contour models. International Journal of Computer Vision 1988;1:321–31.
[7] Adams R, Bischof L. Seeded region growing. IEEE Transactions on Pattern Analysis and Machine Intelligence 1994;16(6):641–7.
[8] Fan J, Yau D, Elmagarmid A, Aref W. Automatic image segmentation by integrating color-edge extraction and seeded region growing. IEEE Transactions on Image Processing 2001;10(10):1454–66.
[9] Pohle R, Behlau T, Töennies K. Segmentation of 3-D medical image data sets with a combination of region based initial segmentation and actives surfaces. Proceedings of SPIE Medical Imaging 2003;5032:1225–32.
[10] Freixenet J, Muñoz X, Raba D, Marti J, Cufi X. Yet another survey on image segmentation: region and boundary information integration, ECCV 2002, LNCS 2352, Springer-Verlang Berlin Heidelberg; 408–422.
[11] Yu Z, Zhu Y, Yang J, Zhu Y. A hybrid region-boundary model for cerebral cortical segmentation in MRI. Computerized Medical Imaging and Graphics 2006;30:197–208.
[12] Lorensen W, Cline H. Marching cubes a high resolution 3D surface reconstruction algorithm. Computer Graphics 1987;21(4):163–9.
[13] Strauss E, Jimenez W, Giraldi G, Silva R, Oliveira A. A semi-automatic surface reconstruction framework based on T-surfaces and isosurface extraction methods. In: XV Brazilian symposium on computer graphics and image processing (SIBGRAPI '02). 2002. p. 24.

[14] Chen T, Metaxas D. A hybrid framework for 3D medical image segmentation. Medical Image Analysis 2005;9:547–65.
[15] Cohen L. On active contour models and balloons. CVGIP: Image Understanding 1991;53(2):211–8.
[16] Xu C, Prince J. Snakes, shapes and gradient vector flow. IEEE Transactions on Image Processing 1998;7:359–69.
[17] McInerney T, Terzopoulos D. Topologically adaptable snakes. In: Proc. of the fifth int. conf. on computer vision. 1995. p. 840–5.
[18] McInerney T, Terzopoulos D. Topology adaptive deformable surfaces for medical image volume segmentation. IEEE Transactions on Medical Imaging 1999;18(10):840–50.
[19] Lin Z, Jin J, Talbot H. Unseeded region growing for 3D image segmentation. ACM International Conference Proceeding Series 2000;9:31–7.
[20] Olabarriaga S, Smeulders A. Interaction in the segmentation of medical images: a survey. Medical Image Analysis 2001;5:127–42.
[21] Cohen M, Painter J, Mehta M, Ma K. Volume seedlings. In: Proceedings of the ACM symposium on interactive 3D graphics. 1992. p. 139–45.
[22] Kim D, Chung S, Park J. Automatic navigation path generation based on two-phase adaptive region-growing algorithm for virtual angioscopy. Medical Engineering and Physics 2006;28:339–47.
[23] Chen Z, Molloi S. Automatic 3D vascular tree construction in CT angiography. Computerized Medical Imaging and Graphics 2003;27:469–79.
[24] Hahn H, Preim B, Selle D, Peitgen H. Visualization and interaction techniques for the exploration of vascular structures. In: Proceedings of visualization conference. 2001. p. 395–402.
[25] Kiraly A, Higgins W, McLennan G, Hoffman E, Reinhardt J. Three-dimensional human airway segmentation methods for clinical virtual bronchoscopy. Academic Radiology 2002;9(10):1153–68.
[26] Zhou X, Hayashi T, Hara T, Fujita H, Yokohama R, Kiryu T, et al. Automatic segmentation and recognition of anatomical lung structures from high-resolution chest CT images. Computerized Medical Imaging and Graphics 2006;30:299–313.
[27] Thiran J, Warscotte V, Macq B. A queue-based region growing algorithm for accurate segmentation of multi-dimensional digital images. Signal Processing 1997;60:1–10.
[28] Xu C, Pham D, Rettmann M, Yu D, Prince J. Reconstruction of the human cerebral cortex from magnetic resonance images. IEEE Transactions on Medical Imaging 1999;18(6):467–80.
[29] Hojjatoleslami S, Kruggel F. Segmentation of large brain lesions. IEEE Transactions on Medical Imaging 2001;20(7):666–9.
[30] Taubin G. A signal processing approach to fair surface design. In: Computer graphics proceedings. 1995. p. 351–8.
[31] Amini A, Weymouth T, Jain R. Using dynamic programming for solving variational problems in vision. IEEE Transactions on Pattern Analysis and Machine Intelligence 1990;12(9):855–67.
[32] Cohen L, Cohen I. Finite-element methods for active contour models and balloons for 2-D and 3-D images. IEEE Transactions on Pattern Analysis and Machine Intelligence 1993;15(11):1131–47.
[33] Collins D, Zijdenbos A, Kollokian V, Sled J, Kabani N, Holmes C, et al. Design and construction of a realistic digital brain phantom. IEEE Transactions on Medical Imaging 1998;17(3):463–8.
[34] Pichon E, Tannenbaum A, Kikinis R. A statistically based surface evolution method for medical image segmentation: presentation and validation. MICCAI 2003;2:711–20.
[35] Yoo TS, Ackerman MJ, Lorensen WE, Schroeder W, Chalana V, Aylward S, et al. Engineering and algorithm design for an image processing Api: a technical report on ITK—the Insight Toolkit. Studies in Health Technology and Informatics 2000;85:586–92.

Mariana del Fresno received her PhD (2008), the MSc (2001) and Systems Engineering (1992) degrees at Universidad Nacional del Centro (Argentina). Currently she is professor in the Department of Computer Science at the same university and member of the technology network PLADEMA (www.pladema.net). Her research interests include medical image processing, digital image segmentation, computer graphics and visualization.

Marcelo Vénere received his PhD (1996) and Engineering degrees (1982) at Instituto Balseiro (Argentina). Currently he is professor of computer science at Universidad Nacional del Centro, and vice-director of the technology network PLADEMA (www.pladema.net). He is a permanent researcher of the National Atomic Energy Commission of Argentina. His research interests involve computer graphics, segmentation and visualization.

Alejandro Clausse received his PhD (1987) and Engineering degrees (1981) at Instituto Balseiro (Argentina). Currently he is professor of computer science at Universidad Nacional del Centro, and director of the technology network PLADEMA (www.pladema.net). He is a permanent researcher of the National S&T Council and the National Atomic Energy Commission of Argentina. His research interests include image processing, information theory and simulation of complex systems.